Taylor & Francis
Taylor & Francis Group

Numerical Heat Transfer, Part A: Applications
An International Journal of Computation and Methodology

ISSN: (Print) (Online) Journal homepage: https://www.tandfonline.com/loi/unht20

Numerical heat transfer of non-similar ternary hybrid nanofluid flow over linearly stretching surface

Saman Riaz, Muhammad F. Afzaal, Zhan Wang, Ahmed Jan & Umer Farooq

To cite this article: Saman Riaz, Muhammad F. Afzaal, Zhan Wang, Ahmed Jan & Umer Farooq (05 Sep 2023): Numerical heat transfer of non-similar ternary hybrid nanofluid flow over linearly stretching surface, Numerical Heat Transfer, Part A: Applications, DOI: 10.1080/10407782.2023.2251093

To link to this article: https://doi.org/10.1080/10407782.2023.2251093

NUMERICAL HEAT TRANSFER, PART A: APPLICATIONS
https://doi.org/10.1080/10407782.2023.2251093

Numerical heat transfer of non-similar ternary hybrid nanofluid flow over linearly stretching surface

Saman Riaz[a], Muhammad F. Afzaal[b], Zhan Wang[b], Ahmed Jan[c], and Umer Farooq[c]*

[a]School of Mathematics and Statistics, Xi'an Jiaotong University, P.R. China; [b]Institute of Mechanics, Chinese Academy of Sciences, Beijing, P.R. China; [c]Department of Mathematics, COMSATS University Islamabad, Pakistan

ABSTRACT

The primary objective of this research is to construct a 2D mathematical model to understand the heat transfer phenomena in a ternary hybrid nanofluid across a stretched surface. We endorsed viscous dissipation formulations in energy equations and the radiation impacts may also be precisely handled by using Rosseland approximation. Nanoparticles and their effects are also considered including Al_2O_3, MgO and TiO_2. The equations used in the model are made nondimensional through non-similarity transformation. In addition, the local non-similarity approach is employed to convert non-similar partial differential equations into ordinary differential equations. These equations can subsequently be solved using the bvp4c MATLAB tool. Key factors have been thoroughly mapped out in graphical form for easy comprehension. In a flow regime, increasing nanoparticle concentration, magnetic number, and Eckert number lowers heat transmission and raises the ternary hybrid nanofluid's temperature profile. The effective skin friction coefficient and Nusselt number are tabulated concerning the aforementioned important factors.

ARTICLE HISTORY
Received 4 May 2023
Revised 25 July 2023
Accepted 2 August 2023

KEYWORDS
Local non-similarity: Bvp4c; ternary hybrid nanofluid; Williamson fluid model

1. Introduction

Magnetohydrodynamics (MHD) is a topic of immense interest both in academia and industry due to its wide range of practical applications that include chemical processing, cooling of vehicles, preservation of digital chips, and extraction of heat from nuclear power plants. Rashidi et al. [1] investigated boundary layer flows in a magnetic field over a spinning disk at a steady state with the aid of numerical simulations. Shafiq et al. [2] performed statistical analysis of Williamson fluid under the impact of hydro-magnetic on a porous stretching surface, whereas natural convection was studied by Haq et al. [3] for MHD flow within a curved porous cavity at different wavelengths and temperatures in a partly heated domain. Shekaramiz et al. [4] studied the MHD boundary layer flow of a nanofluid across a stretched sheet. Using finite difference scheme, Ullah et al. [5] examined the effects of magnetic field and Joule heating on a highly viscous hybrid nanofluid consisted of suspensions of copper-alumina nanoparticles in ethylene glycol. Ahmed et al. [6] investigated the heat transfer in ohmic heating by taking into account the flow of a magnetized, time-dependent viscous fluid induced by a spinning disk. MHD boundary layer flow was studied by Cui et al. [7], who used a different kind of analysis than previously

CONTACT Umer Farooq umer_farooq@comsats.edu.pk Department of Mathematics, COMSATS University Islamabad, Park Road, Chak Shahzad, Islamabad, 44000, Pakistan.
*Additional Affiliation: College of Mathematical Science, Harbin Engineering University, Harbin city 150001, Heilongjiang, China.

used to look at forced convection, and the steady buoyant convective boundary layer flow over Maxwell fluids was taken into account by Fayz-Al-Asad et al. [8].

Ternary hybrid nanofluids are of interest as a heat storage technology despite their much better thermal efficiency compared to hybrid nanofluids and nanofluids. The concept of ternary hybrid nanofluids introduced a third generation of heat transfer fluids. The systematization of these fluids is entirely dependent on the mixture of three nanoparticles and based fluids. The stagnation point flow of Williamson fluid in mixed convection MHD was investigated by Nazir et al. [9]. The effects of a Darcy-Forchheimer precursor surface on a ternary hybrid nanofluid as it moves over a nonlinear stretching surface were studied by Gul & Saeed [10]. The rheology of Prandtl fluid was studied alongside the movement of a ternary hybrid nanofluid in a porous media subject to varying magnetic fields by Sohail et al. [11]. A hybrid nanofluid with preliminary stretching sheet and joule dissipation effects was reported by Khashi'ie. et al. [12], and their flow was shown to be a forced convection boundary layer. Using a $Gr - Fe_3O_4 - H_2O$ hybrid nanofluid, Khazayinejad and Nourazar investigated spatial fractional heat transfer and continuous laminar MHD boundary layer flow [13]. An applied magnetic field and thermal generation and absorption effects on Buongiorno's Sisko fluid model were investigated by Jan et al. [14]. A stretched sheet of fluid was modeled by Cui et al. [15] using a Casson fluid model with nanofluids as the magnetized boundary layer. The Researchers had studied nanofluids in a variety of plates and surface dimensions, likely seeing a wide range of effects depending on the specifics of the setup. By coupling fluid motion with magnetic fields, magnetohydrodynamic (MHD) plays a role in regulating boundary layer flow [16–20]. Imtiaz [21] conducted a study to investigate the influence of thermal radiation on the magnetohydrodynamic (MHD) flow of a Maxwell fluid over a bidirectionally stretched surface, and solved nonlinear differential system using shooting method and the RK-5 scheme.

Radiant heat effects are significant in the industry due to their utilization in energy production, solar energy systems, turbines for gas, and diverse propulsion processes in aircraft. An analysis of the flow of nanoparticles across a stretched membrane in 3D MHD was conducted by Nayak [22], taking into account thermal radiation and viscous dispersion effects. The significance of thermal radiation for the MHD interface of a nanofluid over a nonlinear stretching film was investigated by Mahanthesh et al. [23]. Ullah et al. [24] numerically investigate the effects of thermal radiation on heat transfer rate and drag force over a radially stretching surface. This study employed the Carreau fluid model to characterize the fluid behavior. The ohmic heating and thermal radiation in the Banjourno nanofluid were studied by Hayat et al. [25] where they applied finite difference technique to analyze the MHD flow of a Jeffery model across a stretchable cylinder. Lanjwani et al. [26] investigated the stability and dual analysis of the steady-state laminar flow of radiative Casson fluid incorporated with magnetic effects. Reddy et al. [27] explored the transport analysis of Williamson nanofluid with a porous medium. The thermal radiation slip condition and magnetic are also considered. Swalmeh et al. [28] studied the convective boundary layer flow of effective radiation with MHD in a polar nanofluid in a spherical shape. Oreyeni et al. [29] utilized a combination of hybrid magnetite particles (Fe_3O_4) and silver (Ag) to investigate the thermal characterization function in solar-powered ships under the influence of heat radiation, magnetic fields, and viscous dissipation. Heat flow in the thermal boundary layer was evaluated using the Cattaneo-Christov model, whereas the Galerkin weighted residual method (GWRM) was employed as the methodology for analysis.

In this work, aluminum oxide, magnesium oxide and titanium oxide have been chosen due to their distinctive thermal properties. Nanoparticles of metallic oxides, such as Al_2O_3, SiO_2, ZnO, MgO, and TiO_2, are readily soluble in the base fluids; among these metal oxides, Al_2O_3 has strong thermal properties. Pure metallic nanoparticles, such as aluminum, magnesium, and titanium, are known to have a high aspect ratio, a high heat conductivity and a low specific gravity. The nanofluids are unstable for short periods, however, the incorporation of aluminum oxide, titanium oxide and magnesium oxide in the fluids not only ensures long-term stability but also imparts exceptional thermal properties. $Al_2O_3 + MgO + TiO_2$ ternary hybrid and $Al_2O_3 +$

MgO hybrid nanoparticles may be made in this fashion, and the resulting product is very stable. Reviewing the existing research, it becomes clear that the effect of viscous dissipation on the MHD heat and mass transfer flow of $Al_2O_3 + MgO + TiO_2$ ternary hybrid and $Al_2O_3 + MgO$ hybrid nano liquids across a stretched surface *via* a permeable medium have not yet been investigated. In addition, the Local Non-similarity approach [30–33] that we have proposed is not currently being used to clarify the dynamical issue of hybrid nanofluid *via* porous media. The LNS method, in conjunction with the bvp4c up to its second truncation level, yields numerical solutions to nonlinear-coupled PDEs. Relevant results of the topic at hand, obtained by adjusting the appropriate parameters, are explained, and shown visually *via* tables and diagrams.

2. Mathematical modeling

Ternary hybrid nanoparticles are observed in a non-Newtonian Williamson fluid embedded in porous media over a linear stretching surface. The Williamson fluid (Blood) contains three kinds of nanoparticles *(Al_2O_3, MgO, and TiO_2)* and the Magnetic field is assumed normal to the stretching sheet. The stretching sheet velocity is $u = bx$, where b is constant, in the direction of the x-axis. There is no injection/subjection, which means $v = 0$. The use of thermal radiation, joule heating, and viscous dissipation is central to the concept of thermal expansion. The temperature of the free stream and the temperature of the wall are T_∞ and T_w, respectively; heat generation/absorption effect is assumed. According to [9, 34], Williamson fluid rheology is described by the following equations

$$S = -pI + \tau,$$
$$\tau = \left(\mu_\infty + \frac{\mu_o - \mu_\infty}{1 - \sqrt{\dot{\gamma}}}\right) A_1,$$

where S represents the extra stress tensor. The viscosity under restrictive conditions at an infinite shear rate is defined as μ_∞, whereas the one with zero shear rate is μ_0. The first Rivlin Erickson tensor is represented by A_1. Additionally, $\Gamma > 0$ denotes the time constant and $\dot{\gamma}$ is given by

$$\dot{\gamma} = \sqrt{\frac{\pi}{2}}, \quad \pi = trace\left(A_1^2\right).$$

The prevailing notion μ_∞ equals zero and $\dot{\gamma}$ is less than one, resulting in $\tau = \left(\frac{\mu_o}{1 - \sqrt{\dot{\gamma}}}\right) A_1$. Utilizing binomial expansion, this can be expressed as $\tau = \mu_o\left(1 - \sqrt{\dot{\gamma}}\right) A_1$. The geometry of the problem is shown in Figure 1. Using the above assumptions, the flow problem is:

$$\frac{\partial u}{\partial x} + \frac{\partial v}{\partial y} = 0 \tag{1}$$

$$\rho_{thnf}\left(u\frac{\partial u}{\partial x} + v\frac{\partial u}{\partial y}\right) = \mu_{thnf}\left(\frac{\partial^2 u}{\partial y^2}\right) + \mu_{thnf}\sqrt{2}\Gamma\frac{\partial u}{\partial y}\frac{\partial^2 u}{\partial y^2} - \sigma_{thnf}B_0^2 u - \frac{\mu_{thnf}}{K}u, \tag{2}$$

$$\begin{aligned} u\frac{\partial T}{\partial x} + v\frac{\partial T}{\partial y} = {} & \frac{1}{(\rho c_p)_{thnf}}\left(k_{thnf} + \frac{16}{3}\frac{\sigma^* T_\infty^3}{k^*}\right)\frac{\partial^2 T}{\partial y^2} + \frac{\mu_{thnf}}{(\rho c_p)_{thnf}}\left(1 + \frac{\Gamma}{\sqrt{2}}\frac{\partial u}{\partial y}\right)\left(\frac{\partial u}{\partial y}\right)^2 \\ & + \frac{\sigma_{thnf}}{(\rho c_p)_{thnf}}(uB_o)^2 + \frac{\mu_{thnf}}{K(\rho c_p)_{thnf}}\mathrm{u}^2. \end{aligned} \tag{3}$$

with boundary conditions [35, 36]:

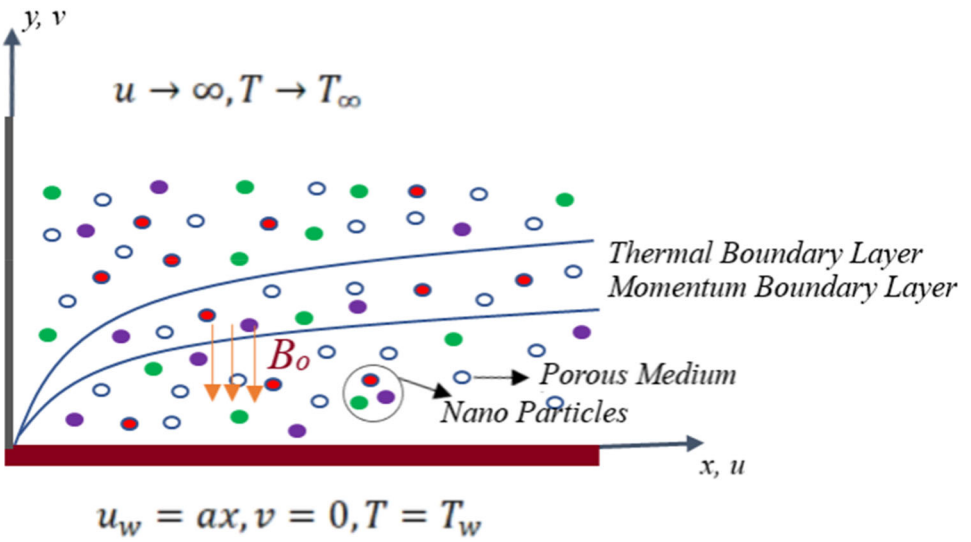

Figure 1. Flow diagram.

$$\begin{aligned} u = bx = u_w(x), v = 0\ ,\ \ T = T_w,\ \ at\ \ y = 0, \\ u = 0 = v,\ \ T \to T_\infty\ \ \ at\ \ y \to \infty. \end{aligned} \tag{4}$$

The variables u and v represent the velocity vectors in the x and y directions, respectively. K, Γ are permeability of porous medium and the Williamson fluid parameter, k^* represents the Boltzmann constant, base fluid density is ρ_f, $(c_p)_f$, T_∞ and T_w indicates base fluid heat capacity ambient and wall temperature. In order to establish a non-similar flow, it is necessary to introduce a new variable denoted as $\xi(x)$ to represent non-similarity, while $\eta(y)$ is used to represent pseudo-similarity variables.

$$\begin{aligned} \xi = \frac{x}{L},\ \ \eta = y\sqrt{\frac{b}{\nu_f}}\ ,\ \ u = bx\frac{\partial f}{\partial \eta}(\xi,\eta),\ \ v = -\sqrt{b\nu_f}\left(f(\xi,\eta) + \xi\frac{\partial f}{\partial \xi}(\xi,\eta)\right), \\ \boldsymbol{\theta}(\ \boldsymbol{\xi},\boldsymbol{\eta}) = \frac{(\boldsymbol{T} - \boldsymbol{T}_\infty)}{(\boldsymbol{T}_w - \boldsymbol{T}_\infty)}. \end{aligned} \tag{5}$$

After applying the aforementioned transformations, Eq. (1) is identically satisfies and the solutions to Eqs. (2)–(4) are the following:

$$\begin{aligned} &\frac{\boldsymbol{\nu}_{thnf}}{\boldsymbol{\nu}_f}\left(1 + \boldsymbol{We}\xi\frac{\partial^2 \boldsymbol{f}}{\partial \boldsymbol{\eta}^2}\right)\frac{\partial^3 \boldsymbol{f}}{\partial \boldsymbol{\eta}^3} - \frac{\boldsymbol{\rho}_f}{\boldsymbol{\rho}_{thnf}}\left(\frac{\boldsymbol{\sigma}_{thnf}}{\boldsymbol{\sigma}_f}\boldsymbol{M} - \boldsymbol{\lambda}\frac{\boldsymbol{\mu}_{thnf}}{\boldsymbol{\mu}_f}\right)\frac{\partial \boldsymbol{f}}{\partial \boldsymbol{\eta}} - \left(\frac{\partial \boldsymbol{f}}{\partial \boldsymbol{\eta}}\right)^2 + \boldsymbol{f}\frac{\partial^2 \boldsymbol{f}}{\partial \boldsymbol{\eta}^2} \\ &\quad = \boldsymbol{\xi}\left(\frac{\partial \boldsymbol{f}}{\partial \boldsymbol{\eta}}\frac{\partial^2 \boldsymbol{f}}{\partial \boldsymbol{\xi}\partial \boldsymbol{\eta}} - \frac{\partial \boldsymbol{f}}{\partial \boldsymbol{\xi}}\frac{\partial^2 \boldsymbol{f}}{\partial \boldsymbol{\eta}^2}\right), \end{aligned} \tag{6}$$

$$\begin{aligned} &\frac{1}{\boldsymbol{Pr}}\left(\frac{\boldsymbol{k}_{thnf}}{\boldsymbol{k}_f} + \boldsymbol{R}_d\right)\frac{\partial^2 \boldsymbol{\theta}}{\partial \boldsymbol{\eta}^2} + \boldsymbol{Ec}\xi^2\left(1 + \boldsymbol{We}\xi\frac{\partial^2 \boldsymbol{f}}{\partial \boldsymbol{\eta}^2}\right)\left(\frac{\partial^2 \boldsymbol{f}}{\partial \boldsymbol{\eta}^2}\right)^2 + \xi^2\boldsymbol{Ec}\left(\frac{\boldsymbol{\sigma}_{thnf}}{\boldsymbol{\sigma}_f}\boldsymbol{M} + \boldsymbol{\lambda}\right)\left(\frac{\partial \boldsymbol{f}}{\partial \boldsymbol{\eta}}\right)^2 \\ &\quad + \frac{(\boldsymbol{\rho c_p})_{thnf}}{(\boldsymbol{\rho c_p})_f}\boldsymbol{f}\frac{\partial \boldsymbol{\theta}}{\partial \boldsymbol{\eta}} = \frac{(\boldsymbol{\rho c_p})_{thnf}}{(\boldsymbol{\rho c_p})_f}\boldsymbol{\xi}\left(\frac{\partial \boldsymbol{f}}{\partial \boldsymbol{\eta}}\frac{\partial \boldsymbol{\theta}}{\partial \boldsymbol{\xi}} - \frac{\partial \boldsymbol{f}}{\partial \boldsymbol{\xi}}\frac{\partial \boldsymbol{\theta}}{\partial \boldsymbol{\eta}}\right), \end{aligned} \tag{7}$$

Transformed boundary conditions are:

$$\frac{\partial f(\xi,0)}{\partial \eta}=1,\ f(\xi,0)+\xi\frac{\partial f(\xi,0)}{\partial \xi}=0,\ \theta(\xi,0)=1,$$
$$\frac{\partial \boldsymbol{f}(\boldsymbol{\xi},\infty)}{\partial \boldsymbol{\eta}}=0,\ \boldsymbol{\theta}(\boldsymbol{\xi},\infty)=0, \tag{8}$$

Weissenberg number $We=\Gamma L\left(\frac{2b^3}{\nu_f}\right)^{\frac{1}{2}}$, magnetic factor $M=\frac{\sigma B_o^2}{b\rho_f}$, porosity factor $\lambda=\frac{\mu_f}{bK\rho_f}$, radiation factor $Rd=\frac{16}{3}\frac{\sigma^* T_\infty^3}{k^* k}$, Eckert number $Ec=\frac{c^2L^2}{C_p(T_w-T_\infty)}$ and Prandtl number $Pr=\frac{\nu_f}{\alpha_f}$.

Surface friction coefficient C_f and local Nusselt number Nu_x are:

$$\boldsymbol{C_f}=\frac{\boldsymbol{\tau_w}}{\frac{1}{2}\boldsymbol{\rho_{thnf}}(\boldsymbol{u_w})^2},\ \boldsymbol{Nu}=\frac{\boldsymbol{xq_w}}{\boldsymbol{k_{nf}}(\boldsymbol{T_w}-\boldsymbol{T_\infty})}, \tag{9}$$

where τ_w surface shear stress, q_w is the surface flux:

$$\boldsymbol{\tau_w}=\boldsymbol{\mu_{thnf}}\left(\frac{\partial \boldsymbol{u}}{\partial \boldsymbol{y}}+\frac{\boldsymbol{\Gamma}}{\sqrt{2}}\left(\frac{\partial \boldsymbol{u}}{\partial \boldsymbol{y}}\right)^2\right)_{\boldsymbol{y}=0},\ \boldsymbol{q_w}=-\left(\boldsymbol{k_{thnf}}+\boldsymbol{Rd}\right)\frac{\partial \boldsymbol{T}}{\partial \boldsymbol{y}}_{\boldsymbol{y}=0}. \tag{10}$$

The dimensionless form of C_f, Nu_x are:

$$\frac{1}{2}\boldsymbol{Re}^{\frac{1}{2}}\boldsymbol{C_f}=\frac{\boldsymbol{\mu_{thnf}}}{\boldsymbol{\mu_f}}\frac{\boldsymbol{\rho_f}}{\boldsymbol{\rho_{thnf}}}\boldsymbol{\xi}^{-1}\left(1+\boldsymbol{\xi We}\frac{\partial^2 \boldsymbol{f}}{\partial \boldsymbol{\eta}^2}(0)\right)\frac{\partial^2 \boldsymbol{f}}{\partial \boldsymbol{\eta}^2}(0),$$
$$\boldsymbol{Re}^{\frac{-1}{2}}\boldsymbol{Nu}=-\xi\left(\frac{\boldsymbol{k_{thnf}}}{\boldsymbol{k_f}}+\boldsymbol{Rd}\right)\frac{\partial \boldsymbol{f}}{\partial \boldsymbol{\eta}}(0). \tag{11}$$

Where $Re=\frac{bL^2}{\nu_f}$

3. Methodology

To tackle the problem of boundary layer nanofluid flow over a stretched surface, the LNS method is used for the dimensionless governing model given in Eqs. (6)–(8) and the imposed boundary conditions (9). The next subsection will provide the step-by-step details of the LNS approach for solving the problem stated above.

3.1. First level truncation

Presumably, ($\xi \ll 1$) exhibits this behavior given that the term $\xi\frac{\partial(.)}{\partial \xi}$ are very small at the first level of truncation. This results in the following forms for Eqs. (6)–(8):

$$\frac{\boldsymbol{\nu_{thnf}}}{\boldsymbol{\nu_f}}\left(1+\boldsymbol{We}\xi \boldsymbol{f}''\right)\boldsymbol{f}''' -\frac{\boldsymbol{\rho_f}}{\boldsymbol{\rho_{thnf}}}\left(\frac{\boldsymbol{\sigma_{thnf}}}{\boldsymbol{\sigma_f}}\boldsymbol{M}-\boldsymbol{\lambda}\frac{\boldsymbol{\mu_{thnf}}}{\boldsymbol{\mu_f}}\right)\boldsymbol{f}' -\boldsymbol{f}'^2+\boldsymbol{f}\boldsymbol{f}''=0, \tag{12}$$

$$\frac{1}{\boldsymbol{Pr}}\left(\frac{\boldsymbol{k_{thnf}}}{\boldsymbol{k_f}}+\boldsymbol{R_d}\right)\boldsymbol{\theta}''+\boldsymbol{Ec}\xi^2\left(1+\boldsymbol{We}\xi \boldsymbol{f}''\right)\boldsymbol{f}''^2+\xi^2\boldsymbol{Ec}\left(\frac{\boldsymbol{\sigma_{thnf}}}{\boldsymbol{\sigma_f}}\boldsymbol{M}+\boldsymbol{\lambda}\frac{\boldsymbol{\mu_{thnf}}}{\boldsymbol{\mu_f}}\right)\boldsymbol{f}'^2+\frac{(\boldsymbol{\rho c_p})_{\boldsymbol{thnf}}}{(\boldsymbol{\rho c_p})_{\boldsymbol{f}}}\boldsymbol{f}\boldsymbol{\theta}'=0, \tag{13}$$

accompanying by boundary conditions:

$$f'(\xi,0)=1,\ f(\xi,0)=0,\ \theta(\xi,0)=1,\\ f'(\xi,\infty)=0,\ \theta(\xi,\infty)=0. \tag{14}$$

3.2. Second level truncation

To obtain the 2nd order truncation, differentiating Eqs. (6)–(8) concerning ξ and introducing new functions $g(\xi,\eta)=\frac{\partial f(\xi,\eta)}{\partial \xi}$, $h(\xi,\eta)=\frac{\partial \theta(\xi,\eta)}{\partial \xi}$, and put the ξ derivatives of the introducing function equal to zero as $\frac{\partial g(\xi,\eta)}{\partial \xi}=\frac{\partial h(\xi,\eta)}{\partial \xi}=0$. The transformed equations are:

$$g''=\frac{1}{\frac{\nu_{thnf}}{\nu_f}(1+We\xi f'')}\left[\frac{\nu_{thnf}}{\nu_f}\left(Wef''f'''+We\xi g''f'''\right)-3f'g'+f''g'+g''f'\right.\\ \left.-\frac{\rho_f}{\rho_{thnf}}\left(\frac{\sigma_{thnf}}{\sigma_f}M+\lambda\right)f'+gf''-\xi\left(g'^2-gg''\right)\right] \tag{15}$$

$$\left(\frac{k_{thnf}}{k_f}+R_d\right)\theta''=\left[2Ec\xi\left(1+We\xi f''\right)f''^2+2Ec\xi^2\left(1+We\xi f''\right)f''g''+Ec\xi^2g''f''^2\right.\\ \left.+2\xi Ec\left(\frac{\sigma_{thnf}}{\sigma_f}M+\lambda\right)f''^2+\frac{(\rho c_p)_{thnf}}{(\rho c_p)_f}f\theta'+\frac{(\rho c_p)_{thnf}}{(\rho c_p)_f}\left\{\left(f'h-g\theta'\right)+\xi\left(g'h-gh'\right)\right\}\right] \tag{16}$$

with boundary conditions:

$$g'(0)=0,\ g(0)=0,\ h(0)=0,\\ g'(\infty)=0,\ h(\infty)=0. \tag{17}$$

4. Results and discussion

In this article, a non-similar model is designed, and the LNS approach is implemented *via* a bvp4c MATLAB-based algorithm to achieve a numerical solution. After resolving the governing system numerically, the outcomes obtained are depicted in figures and tables. This study centres on a ternary hybrid nanofluid flow model comprising Blood the base fluid along with alumina (Al_2O_3), magnesium oxide (MgO), and titanium dioxide (TiO_2) [38, 39] nanoparticles to exemplify its characteristics. Table 1 elucidates the correlations employed in ternary hybrid nanofluid formulation [37], while Table 2 delineates the numerical attributes of alumina (Al_2O_3), magnesium oxide (MgO), and titanium dioxide (TiO_2) nanoparticles. To verify the applied method and present the accuracy, the results are compared with the previous studies [40, 41] through Table 3. Computational findings of the drag coefficient and heat transfer rate for the considered nanofluids ($Al_2O_3-Williamson\ fluid$, $Al_2O_3+MgO-Williamson\ fluid$ and $Al_2O_3+MgO+TiO_2-Williamson\ fluids$ are presented in Tables 4 and 5. In Table 4, it is clear that the drag coefficient increases when new values of the magnetic parameter (M) and the porosity parameter (λ) are found. It is observed that increasing the values of M and λ leads to a decrease in skin friction decreases, while We increases. From the analysis presented in Table 5, it is evident that higher values of the radiation parameter (Rd) and Weissenberg number (We) result in an increase in Nusselt number. On the other hand, accumulated estimations of porosity parameter (λ), magnetic number (M), and Eckert number (Ec) are responsible to reduce the Nusselt Number. Notably, the $Al_2O_3+MgO+TiO_2-Williamson\ fluid$ exhibits a more pronounced influence on both skin friction and Nusselt number compared to $Al_2O_3+Mg-Williamson\ fluid$ and $Al_2O_3-Williamson\ fluid$.

Table 1. Model of thermophysical properties [37].

Viscosity

nanofluid

$$\mu_{(Al_2O_3)Blood} = \frac{\mu_{blood}}{\left(1-\phi_{Al_2O_3}\right)^{2.5}}$$

hybrid nanofluid

$$\mu_{(Al_2O_3+MgO)Blood} = \frac{\mu_f}{\left(1-\phi_{Al_2O_3}\right)^{2.5}\left(1-\phi_{MgO}\right)^{2.5}}$$

ternary hybrid nanofluid

$$\mu_{(Al_2O_3+MgO+TiO_2)Blood} = \frac{\mu_f}{\left(1-\phi_{Al_2O_3}\right)^{2.5}\left(1-\phi_{MgO}\right)^{2.5}\left(1-\phi_{TiO_2}\right)^{2.5}}$$

Density

nanofluid

$$\rho_{(Al_2O_3)Blood} = \left(1-\phi_{Al_2O_3}\right)\rho_{Blood} + \phi_{Al_2O_3}\rho_{Al_2O_3}$$

hybrid nanofluid

$$\rho_{(Al_2O_3+MgO)Blood} = \left(1-\phi_{MgO}\right)\left(\left(1-\phi_{Al_2O_3}\right)\rho_{Blood} + \phi_{Al_2O_3}\rho_{Al_2O_3}\right) + \phi_{MgO}\rho_{MgO}$$ ternary hybrid nanofluid

$$\rho_{(Al_2O_3+MgO+TiO_2)Blood} = \left(1-\phi_{TiO_2}\right)\left(\left(1-\phi_{MgO}\right)\left(\left(1-\phi_{Al_2O_3}\right)\rho_{Blood} + \phi_{Al_2O_3}\rho_{Al_2O_3}\right) + \phi_{MgO}\rho_{MgO}\right) + \phi_{MgO}\rho_{TiO_2}$$

Heat capacitance

nanofluid

$$(\rho c_p)_{(Al_2O_3)Blood} = \left(1-\phi_{Al_2O_3}\right)(\rho c_p)_{Blood} + \phi_{Al_2O_3}(\rho c_p)_{Al_2O_3}$$ hybrid nanofluid

$$(\rho c_p)_{(Al_2O_3+MgO)Blood} = \left(1-\phi_{MgO}\right)\left(\left(1-\phi_{Al_2O_3}\right)(\rho c_p)_{Blood} + \phi_{Al_2O_3}(\rho c_p)_{Al_2O_3}\right) + \phi_{MgO}(\rho c_p)_{MgO}$$

ternary hybrid nanofluid

$$(\rho c_p)_{(Al_2O_3+MgO+TiO_2)Blood} = \left(1-\phi_{TiO_2}\right)\left(\left(1-\phi_{MgO}\right)\left(\left(1-\phi_{Al_2O_3}\right)(\rho c_p)_{Blood} + \phi_{Al_2O_3}(\rho c_p)_{Al_2O_3}\right) + \phi_{MgO}(\rho c_p)_{MgO}\right) + \phi_{TiO_2}(\rho c_p)_{TiO_2}$$

Electric conductivity

nanofluid

$$\frac{\sigma_{(Al_2O_3)Blood}}{\sigma_{Blood}} = \frac{\sigma_{Al_2O_3}+2\sigma_{Blood}-2\phi_{Al_2O_3}\left(\sigma_{Blood}-\sigma_{Al_2O_3}\right)}{\sigma_{Al_2O_3}+2\sigma_{Blood}+\phi_{Al_2O_3}\left(\sigma_{Blood}-\sigma_{Al_2O_3}\right)}$$

hybrid nanofluid

$$\frac{\sigma_{(Al_2O_3-MgO)Blood}}{\sigma_{(Al_2O_3)Blood}} = \frac{\sigma_{MgO}+2\sigma_{(Al_2O_3)Blood}-2\phi_{MgO}\left(\sigma_{(Al_2O_3)Blood}-\sigma_{MgO}\right)}{\sigma_{MgO}+2\sigma_{(Al_2O_3)Blood}+\phi_{MgO}\left(\sigma_{(Al_2O_3)Blood}-\sigma_{MgO}\right)}$$

ternary hybrid nanofluid

$$\frac{\sigma_{(Al_2O_3-MgO-TiO_2)Blood}}{\sigma_{(Al_2O_3-MgO)Blood}} = \frac{\sigma+2\sigma_{(Al_2O_3-MgO)Blood}-2\phi_{TiO_2}\left(\sigma_{(Al_2O_3-MgO)Blood}-\sigma_{TiO_2}\right)}{\sigma_{TiO_2}+2\sigma_{(Al_2O_3-MgO)Blood}+\phi_{TiO_2}\left(\sigma_{(Al_2O_3-MgO)Blood}-\sigma_{TiO_2}\right)}$$

Thermal conductivity

nanofluid

$$\frac{k_{(Al_2O_3)Blood}}{k_{Blood}} = \frac{k_{Al_2O_3}+2k_{Blood}-2\phi_{Al_2O_3}\left(k_{Blood}-k_{Al_2O_3}\right)}{k_{Al_2O_3}+2k_{Blood}+\phi_{Al_2O_3}\left(k_{Blood}-k_{Al_2O_3}\right)}$$

hybrid nanofluid

$$\frac{k_{(Al_2O_3-MgO)Blood}}{k_{(Al_2O_3)Blood}} = \frac{k_{MgO}+2k_{(Al_2O_3)Blood}-2\phi_{MgO}\left(k_{(Al_2O_3)Blood}-k_{MgO}\right)}{k_{MgO}+2k_{(Al_2O_3)Blood}+\phi_{MgO}\left(k_{(Al_2O_3)Blood}-k_{MgO}\right)}$$

ternary hybrid nanofluid

$$\frac{k_{(Al_2O_3-MgO-TiO_2)Blood}}{k_{(Al_2O_3-MgO)Blood}} = \frac{k_{TiO_2}+2k_{(Al_2O_3-MgO)Blood}-2\phi_{TiO_2}\left(k_{(Al_2O_3-MgO)Blood}-k_{TiO_2}\right)}{k_{TiO_2}+2k_{(Al_2O_3-MgO)Blood}+\phi_{TiO_2}\left(k_{(Al_2O_3-MgO)Blood}-k_{TiO_2}\right)}$$

Table 2. Properties of the Al_2O_3 (Aluminum Oxide), MgO (Magnesium oxide), TiO_2 (Titanium Oxide) and water [38, 39].

Materials	c_p (J/kgK)	ρ (kg/m3)	k(W/mK)	$\sigma(\Omega m)^{-1}$
Al2O3	765	3970	40	36.9×10^6
MgO	960	3580	48.4	2.4×10^6
TiO2	686.2	4250	8.9538	2.38×10^6
Blood	3594	1063	0.492	0.8

Table 3. A comparison of the $\frac{\partial f}{\partial \eta}(0)$ with published literature for different values of *Pr*, putting $M = \lambda = We = Ec = \phi_1 = \phi_2 = \phi_3 = Rd = 0$ and $\xi = 0.1$.

Pr	Golra and Sidawi [40]	Megahed [41]	Present study
0.007	0.06562	0.065531	0.1222647925
0.2	0.16912	0.169117	0.2529709253
2.0	0.91142	0.911358	0.9804025184
7.0	1.89546	1.895453	1.9240861311
20.0	3.35391	3.353902	3.3227827227

Table 4. Computed values of $Re^{\frac{1}{2}}C_f$ for various values of *M*, λ, and *We*.

M	λ	*We*	$Re^{\frac{1}{2}}C_f Al_2O_3$ −*Williamson fluid*	$Re^{\frac{1}{2}}C_f Al_2O_3 + MgO$ −*Williamson fluid*	$Re^{\frac{1}{2}}C_f Al_2O_3 + MgO + TiO_2$ −*Williamson fluid*
0.1	0.1	0.1	−0.5085659092	−0.5379949862	−0.5746465827
0.3			−0.5413009524	−0.5636778551	−0.6052535964
0.6			−0.5860588976	−0.5997018210	−0.6479427472
0.1	0.1		−0.5085659092	−0.5379949862	−0.5746465827
	0.5		−0.3970596958	−0.4301016854	−0.4663653380
		0.1	−0.5085659092	−0.5379949862	−0.5746465827
		0.5	−0.5800153955	−0.6228564221	−0.6730519213

Table 5. Computed values of $Re^{-\frac{1}{2}}Nu$ for various values of ϕ, *M*, *Q*, *Rd*, *Ec*, and *Pr*.

M	λ	*Rd*	*Ec*	*We*	$Re^{-\frac{1}{2}}NuAl_2O_3$ *Williamson fluid*	$Re^{-\frac{1}{2}}NuAl_2O_3 +$ *Williamson fluid*	$Re^{-\frac{1}{2}}NuAl_2O_3 + MgO + TiO_2$ *Williamson fluid*
0.3	0.3	0.2	0.1	0.1	1.6870981029	1.5602713933	1.5385418163
0.6					1.7552725974	1.5786816550	1.5578544907
0.3	0.3				1.6870981029	1.5602713933	1.5385418163
	0.5				1.7265128258	1.5765272268	1.5551905718
		0.2			1.6870981029	1.5602713933	1.5385418163
		0.4			1.3670819963	1.2757618076	1.2588423127
			0.10		1.6870981029	1.5602713933	1.5385418163
			0.13		1.9491890064	1.7960665079	1.7706423250
				0.1	1.6870981029	1.5602713933	1.5385418163
				0.2	1.6681925746	1.5591472865	1.5374987246

The Darcy parameter is used to study the resistance a porous Darcy media poses to the flow of $Al_2O_3 + MgO + TiO_2 - Williamson\ fluid$, $Al_2O_3 + MgO - Williamson\ fluid$, and $Al_2O_3 - Williamson\ fluid$. An increase in the Darcy porous medium parameter correlates to a reduction in the permeability of the porous, which causes a significant slowing of the fluid's motion. According to Darcy's model, the resistance of a porous medium is proportional to its permeability; so, a reduction in permeability indicates an increase in porous medium resistance, which in turn slows down the movement of fluids inside the porous medium. Additionally, if the fluid is pushed through a porous media with extremely low permeability, the BL thickness may be decreased to the required value. In Figure 2, it is also noticed that the Boundary Layer thickness for $Al_2O_3 + MgO + TiO_2 -$ Williamson fluid is greater than the thickness of the Boundary Layer associated with the flow of $Al_2O_3 + MgO -$ Williamson fluid and Al_2O_3-Williamson fluid. It means that $l_2O_3 + MgO + TiO_2 -$ Williamson fluid experience more porous medium resistance relative to $Al_2O_3 + MgO - Williamson\ fluid$ and Al_2O_3-Williamson fluid. Figure 3 depicts the effects of the magnetic field on the velocity profile. By applying transverse magnetite fields produce Lorentz forces, which are resistive forces, when applied orthogonally to a flow direction. Because the Lorentz force resists the flow of fluid, the velocity decreases, thereby slowing down fluid flow in the boundary layer. This result quantitatively matches what we expected since magnetic fields retard natural convection flow. Figure 4 displays the results of numerical simulations

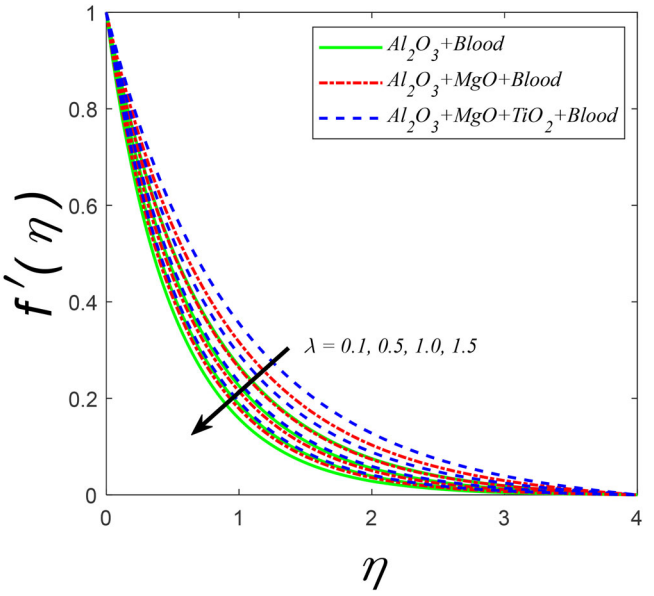

Figure 2. Effect of α on $f'(\eta)$, when $M = 0.3$, $We = 0.5, \phi_1 = \phi_2 = \phi_3 = 0.1$, $Pr = 21$, $Ec = 0.1$, $Q = 0.8$, and $Rd = 0.1$.

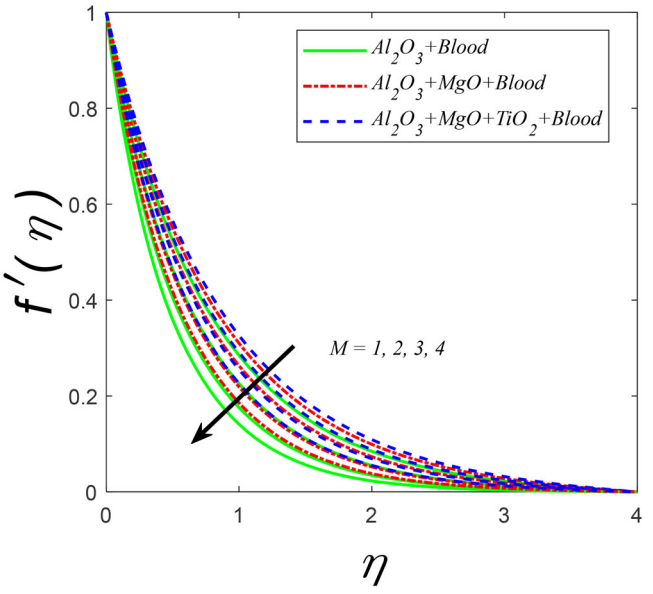

Figure 3. Effect of M on $f'(\eta)$, when $\lambda = 0.2$, $We = 0.5, \phi_1 = \phi_2 = \phi_3 = 0.1$, $Pr = 21$, $Ec = 0.1$, $Q = 0.8$, and $Rd = 0.1$.

of fluid particle motion as a function of the Weissenberg number. It can be seen that the fluid motion slows down with larger values of the Weissenberg number. The viscosity of a fluid increases as the We number is increased, which is the ratio between the viscous force and the elastic force. Due to this force attenuation, the particles in a fluid have a greater increase in viscosity. Increasing the We number lessens the thickness of the boundary layers. This is true of all three types of Williamson fluids: $Al_2O_3 + MgO + TiO_2 - Williamson\ fluid$, $Al_2O_3 + MgO - Williamson\ fluid$, and $Al_2O_3 - Williamson\ fluid$. It is also observed that $Al_2O_3 + MgO + TiO_2 - Williamson\ fluid$ has a larger retardation in fluid motion compared to $Al_2O_3 + MgO - Williamson\ fluid$ and $Al_2O_3 -$

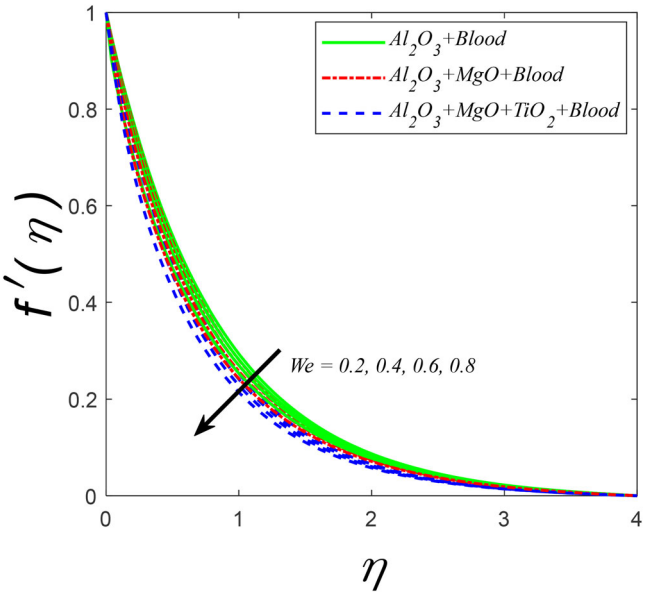

Figure 4. Effect of *We* on $f'(\eta)$, when, $\lambda = 0.2$, $PM = 0.3, \phi_1 = \phi_2 = \phi_3 = 0.1$, $Pr = 21$, $Ec = 0.1$, $Q = 0.8$, and $Rd = 0.1$.

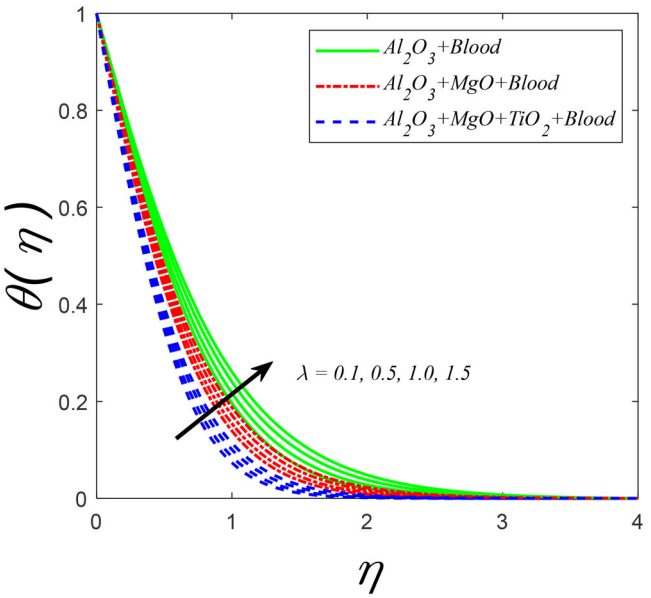

Figure 5. Effect of α on $\theta(\eta)$, when $M = 0.3$, $We = 0.5, \phi_1 = \phi_2 = \phi_3 = 0.1$, $Pr = 21$, $Ec = 0.1$, $Q = 0.8$, and $Rd = 0.1$.

Williamson fluid. It follows that a higher Weissenberg number fluid may be used to decrease the thickness of the boundary layer (BL).

Figure 5 depicts the temperature field's change for porosity parameter values. As the porosity parameter is increased for the nanofluid ($Al_2O_3 - Williamson\ fluid$) hybrid nanofluid ($Al_2O_3 + MgO$-Williamson fluid) and ternary hybrid nanofluid ($Al_2O_3 + MgO + TiO_2$-*Williamson fluid*), it is seen that the temperature rises. When the porosity is high, fluid particles are propelled downward, where the temperature is higher. Figure 6 shows comparative scrutiny of the temperature profile $\theta(\eta)$ of nano, hybrid, and ternary hybrid fluid for numerous measurements of the magnetic parameter (M). Figure 6 demonstrates that the $\theta(\eta)$ of the nanofluid grows with

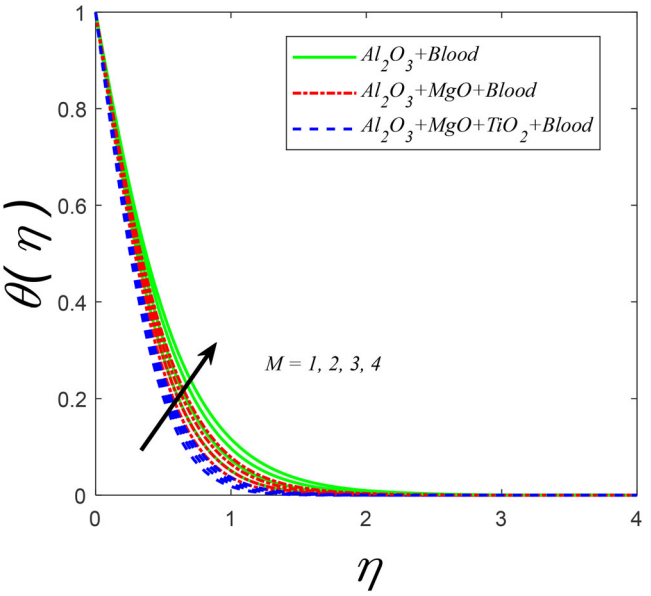

Figure 6. Effect of M on $\theta(\eta)$, when $\lambda = 0.2$, $We = 0.5, \phi_1 = \phi_2 = \phi_3 = 0.1$, $Pr = 21$, $Ec = 0.1$, $Q = 0.8$, and $Rd = 0.1$.

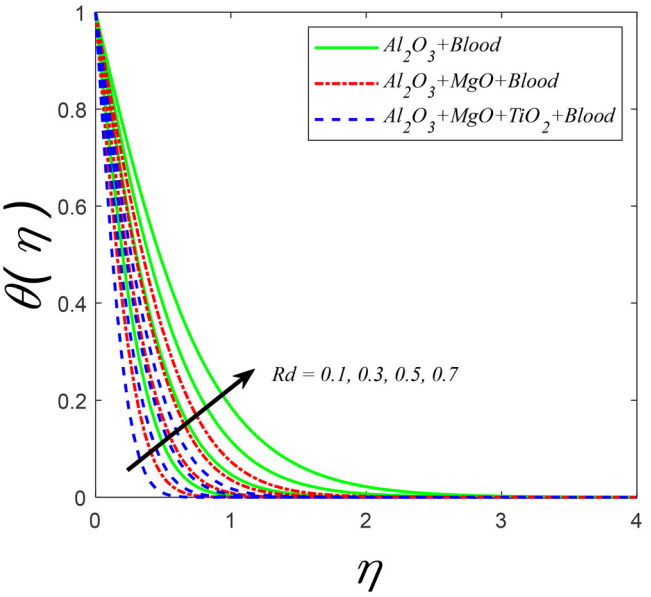

Figure 7. Effect of Rd on $\theta(\eta)$, when $\lambda = 0.2, M = 0.3$, $We = 0.5, \phi_1 = \phi_2 = \phi_3 = 0.1$, $Pr = 21$, $Ec = 0.1$, and $Q = 0.8$.

the increasing estimations of M. Physically, this is because of the Lorentz force generated by the magnetic field, which retards velocity and improves the uniformity of the thermal boundary layer. As the indented graph demonstrates, the temperature distribution of nanofluid $(Al_2O_3 - Williamson\ fluid)$ and hybrid nanofluid $(Al_2O_3 + MgO - Williamson\ fluid)$ is continually lower than that of ternary hybrid nanofluid $(Al_2O_3 + MgO + TiO_2 - Williamson\ fluid)$. Figure 7 demonstrates that when the radiation parameter (Rd) is raised, the thermal boundary layer thickens. When examining the data, this becomes evident. This is because the boundary layer is heated by the imposition of thermal radiation, leading to a rise in fluid temperature. This explains why this is happening. Eckert number (Ec) influence on the thermal boundary layer, as seen in Figure 8. The

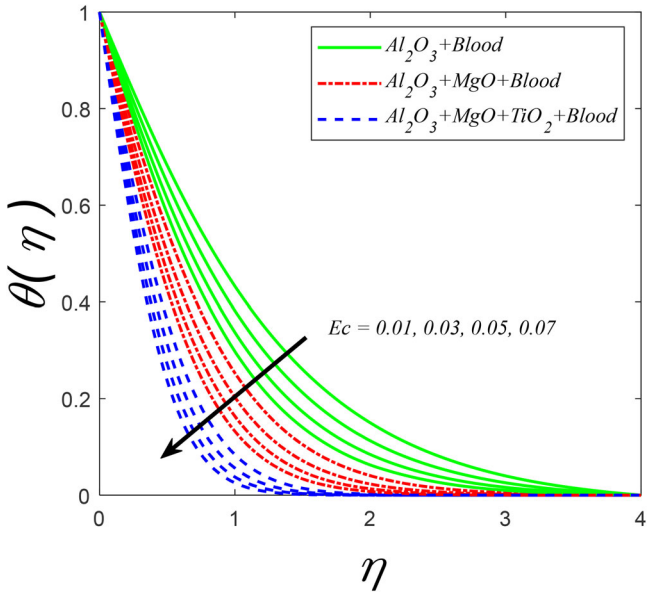

Figure 8. Effect of *Ec* on $\theta(\eta)$, when $\lambda = 0.2, M = 0.3$, $We = 0.5, \phi_1 = \phi_2 = \phi_3 = 0.1$, $Pr = 21$, $Q = 0.8$ and $Rd = 0.1$.

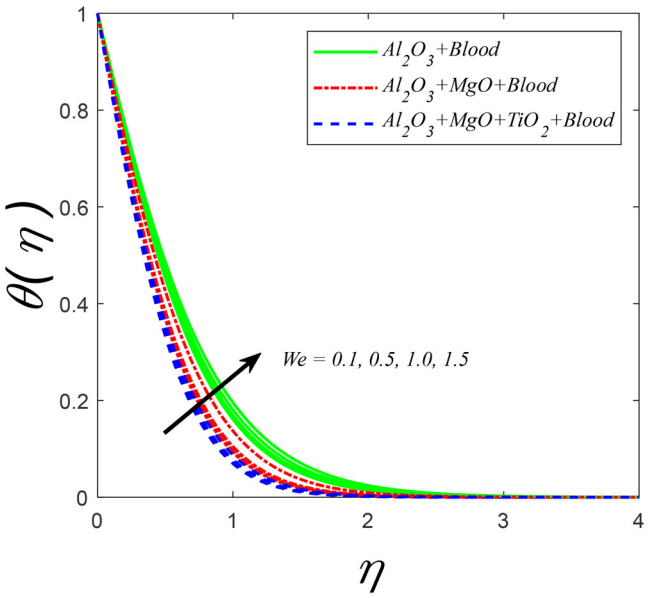

Figure 9. Effect of *Rd* on $\theta(\eta)$, when $= 0.2, M = 0.3$, $\lambda = 0.2, \phi_1 = \phi_2 = \phi_3 = 0.1$, $Pr = 21$, $Ec = 0.1$, and $Q = 0.8$.

Ec number first showed up as a coefficient of the viscous dissipation term, suggesting that this is the mechanism through which it first arose. The rate of work done, or viscous dissipation, increases with large values of *Ec*. Work done is also put to use in the motion of fluid particles, and it helps to increase the internal energy of fluid particles. However, particle temperatures were rising at the same time. To calculate the kinetic energy of moving $Al_2O_3 + MgO - Williamson\ fluid$, $Al_2O_3 - Williamson\ fluid$, and $Al_2O_3 + MgO + TiO_2 - Williamson\ fluid$ the parameter *Ec* is used. The *Ec* is used to communicate enthalpy fluctuations across boundary layers associated with thermal energy, and it is largely used to analyze the rate of heat dissipation in the motion of fluid particles. The effect of a rising Weissenberg number on the temperature is seen in Figure 9. A temperature

rise is indicated by an increase in the Weissenberg number. The duration of relaxation divided by the time of retardation yields the Weissenberg number. As the retardation time decreases, the Weissenberg number increases, and the thermal boundary layer extends more in $Al_2O_3 + MgO + TiO_2 - Williamson\ fluid$ than in $Al_2O_3 + MgO - Williamson\ fluid$ or $Al_2O_3 - Williamson\ fluid$.

5. Conclusion

In this investigation, we examined the Williamson fluid model with magnetic, and thermal radiation impacts on nanofluid, hybrid nanofluid, and ternary hybrid nanofluid flow embedded in porous media over a linear stretching surface. The resultant set of nondimensional equations is solved using a local non-similarity (LNS) strategy up to the second truncation level through the bvp4c MATLAB tool. Additionally, the effects of several developing factors have been fully covered. The followings are the primary findings of the current investigation:

- For $Al_2O_3 + MgO + TiO_2 - Williamson\ fluid$, $Al_2O_3 + MgO - Williamson\ fluid$ and $Al_2O_3 - Williamson\ fluid$ flows, λ has a significant effect on the momentum boundary layer's thickness. As the value of λ increased and the velocity profile decreased, the thermal boundary layer became more effective. Additionally, this influence skin friction and the rate of heat transmission. With a rise in temperature, heat conduction is accelerated and skin friction is reduced.
- The Weissenberg number plays a significant role in determining the momentum boundary layer thickness for $Al_2O_3 + MgO + TiO_2 - Williamson\ fluid$, $Al_2O_3 + MgO - Williamson\ fluid$, and $Al_2O_3 - Williamson\ fluid$ flows. The thickness of the boundary layer for a Williamson fluid exhibits notable differences in comparison to that of a Newtonian fluid. The boundary layer thickness of Williamson fluid exhibits an intriguing contrast in comparison to that of Newtonian fluid.
- Simulated flows of $Al_2O_3 + MgO + TiO_2 - Williamson\ fluid$ show a larger Lorentz force compared to those of $Al_2O_3 + MgO - Williamson\ fluid$ and $Al_2O_3 + -Williamson\ fluid$. Therefore, the flow of $Al_2O_3 + MgO + TiO_2 - Williamson\ fluid$ has a thinner momentum boundary layer than that of $Al_2O_3 + MgO - Williamson\ fluid$ and $Al_2O_3 - Williamson\ fluid$, respectively. As a result, the $Al_2O_3 + MgO + TiO_2 - Williamson\ fluid$ causes a smaller change in magnetic flux owing to distortion of magnetic lines than the $Al_2O_3 + MgO - Williamson\ fluid$ and the $Al_2O_3 - Williamson\ fluid$.
- It is noticed that the coefficient of convective heat transfer depreciates for the rising values of Eckert number have significant effects on $Al_2O_3 - Williamson\ fluid$, and $Al_2O_3 + MgO - Williamson\ fluid$ has compared to that of $Al_2O_3 + MgO + TiO_3 - Williamson\ fluid$.

Numerical simulations reveal that the skin friction associated with $Al_2O_3 + MgO + TiO_2 - Williamson\ fluid$ is higher than that of $Al_2O_3 + MgO - Williamson\ fluid$ and $Al_2O_3 + Williamson\ fluid$ with the same composition. Additionally, the drag force is found to increase as the values of M and We increase, while it decreases with the increase in λ.

ORCID

Umer Farooq http://orcid.org/0000-0002-0920-6174

References

[1] M. M. Rashidi, S. Abelman, and N. F. Mehr, "Entropy generation in steady MHD flow due to a rotating porous disk in a nanofluid," *Int. J. Heat Mass Transf.*, vol. 62, pp. 515–525, 2013. DOI: 10.1016/j.ijheatmasstransfer.2013.03.004.

[2] A. Shafiq and T. N. Sindhu, "Statistical study of hydromagnetic boundary layer flow of Williamson fluid regarding a radiative surface," *Results Phys.*, vol. 7, pp. 3059–3067, 2017. DOI: 10.1016/j.rinp.2017.07.077.

[3] R. U. Haq, F. A. Soomro, T. Mekkaoui, and Q. M. Al-Mdallal, "MHD natural convection flow enclosure in a corrugated cavity filled with a porous medium," *Int. J. Heat Mass Transf.*, vol. 121, pp. 1168–1178, 2018. DOI: 10.1016/j.ijheatmasstransfer.2018.01.063.

[4] M. Shekaramiz, S. Fathi, H. A. Ataabadi, H. Kazemi-Varnamkhasti, and D. Toghraie, "MHD nanofluid free convection inside the wavy triangular cavity considering periodic temperature boundary condition and velocity slip mechanisms," *Int. J. Therm. Sci.*, vol. 170, pp. 107179, 2021. DOI: 10.1016/j.ijthermalsci.2021.107179.

[5] H. Ullah, T. Hayat, S. Ahmad, M. S. Alhodaly, and S. Momani, "Numerical simulation of MHD hybrid nanofluid flow by a stretchable surface," *Chin. J. Phys.*, vol. 71, pp. 597–609, 2021. DOI: https:DOI: 10.1016/j.cjph.2021.03.017.

[6] S. Ahmad, T. Hayat, A. Alsaedi, H. Ullah, and F. Shah, "Computational modeling and analysis for the effect of magnetic field on rotating stretched disk flow with heat transfer," *Propulsion Power Res*, vol. 10, no. 1, pp. 48–57, 2021. DOI: 10.1016/j.jppr.2020.11.005.

[7] J. Cui *et al.*, "Significance of nonsimilar numerical simulations in forced convection from stretching cylinder subjected to external magnetized flow of Sisko fluid," *J. Math.*, vol. 2021, pp. 1–11, 2021. DOI: 10.1155/2021/9540195.

[8] M. Fayz-Al-Asad, T. Oreyeni, M. Yavuz, and P. O. Olanrewaju, "Analytic simulation of MHD boundary layer flow of a chemically reacting upper-convected Maxwell fluid past a vertical surface subjected to double stratifications with variable properties," *Eur. Phys. J. Plus*, vol. 137, no. 7, pp. 1–11, 2022. DOI: 10.1140/epjp/s13360-022-03014-w.

[9] U. Nazir, M. A. Sadiq, and M. Nawaz, "Non-Fourier thermal and mass transport in hybrid nano-Williamson fluid under chemical reaction in Forchheimer porous medium," *Int. Commun. Heat Mass Transf.*, vol. 127, pp. 105536, 2021. DOI: 10.1016/j.icheatmasstransfer.2021.105536.

[10] T. Gul and A. Saeed, "Nonlinear mixed convection couple stress ternary hybrid nanofluids flow in a Darcy–Forchheimer porous medium over a nonlinear stretching surface," *Waves Random Complex Media*, pp. 1–18, 2022. DOI: 10.1080/17455030.2022.2077471.

[11] M. Sohail *et al.*, "Galerkin finite element analysis for the augmentation in thermal transport of ternary-hybrid nanoparticles by engaging non-Fourier's law," *Sci. Rep.*, vol. 12, no. 1, pp. 13497, 2022. DOI: 10.1038/s41598-022-17424-4.

[12] N. S. Khashi'ie, N. M. Arifin, and I. Pop, "Magnetohydrodynamics (MHD) boundary layer flow of hybrid nanofluid over a moving plate with Joule heating," *Alexandria Eng. J.*, vol. 61, no. 3, pp. 1938–1945, 2022. DOI: 10.1016/j.aej.2021.07.032.

[13] M. Khazayinejad and S. S. Nourazar, "On the effect of spatial fractional heat conduction in MHD boundary layer flow using Gr-Fe3O4–H2O hybrid nanofluid," *Int. J. Therm. Sci.*, vol. 172, pp. 107265, 2022. DOI: 10.1016/j.ijthermalsci.2021.107265.

[14] A. Jan, M. Mushtaq, U. Farooq, and M. Hussain, "Nonsimilar analysis of magnetized Sisko nanofluid flow subjected to heat generation/absorption and viscous dissipation," *J. Magnetism Magnetic Mater.*, vol. 564, pp. 170153, 2022. DOI: 10.1016/j.jmmm.2022.170153.

[15] J. Cui, A. Jan, U. Farooq, M. Hussain, and W. A. Khan, "Thermal analysis of radiative Darcy–Forchheimer nanofluid flow across an inclined stretching surface," *Nanomater.*, vol. 12, no. 23, pp. 4291, 2022. DOI: 10.3390/nano12234291.

[16] A. Mathew, S. Areekara, A. S. Sabu, and S. Saleem, "Significance of multiple slip and nanoparticle shape on stagnation point flow of silver-blood nanofluid in the presence of induced magnetic field," *Surfaces Interf.*, vol. 25, pp. 101267, 2021. DOI: 10.1016/j.surfin.2021.101267.

[17] J. Mackolil and M. Basavarajappa, "Thermo-solutal Marangoni convective assisting/resisting flow of a nanofluid with radiative heat flux: a model with heat transfer optimization," *ZAMM-J. Appl. Math. Mech./Zeitschrift Für Angewandte Mathematik Und Mechanik*, vol. 102, no. 11, pp. e202100504, 2022. DOI: 10.1002/zamm.202100504.

[18] M. Basavarajappa and D. Bhatta, "Heat and mass transfer of a molten polymer conveying nanoparticles in a wire coating process with temperature-dependent fluid properties: optimization using response surface method," *Int. Commun. Heat Mass Transf.*, vol. 133, pp. 105941, 2022. DOI: 10.1016/j.icheatmasstransfer.2022.105941.

[19] I. L. Animasaun, T. K. Kumar, F. A. Noah, S. S. Okoya, Q. M. Al-Mdallal, and M. M. Bhatti, "Insight into Darcy flow of ternary-hybrid nanofluid on horizontal surfaces: exploration of the effects of convective and unsteady acceleration," *ZAMM-J. Appl. Math. Mech./Zeitschrift Für Angewandte Mathematik Und Mechanik*, vol. 103, no. 5, pp. e202, 2022. DOI: 10.1002/zamm.202200197.

[20] M. M. Bhatti and R. Ellahi, "Numerical investigation of non-Darcian nanofluid flow across a stretchy elastic medium with velocity and thermal slips," *Numer. Heat Transf., Part B: Fundamentals*, vol. 83, no. 5, pp. 323–343, 2023. DOI: 10.1080/10407790.2023.2174624.

[21] M. Imtiaz, "Impact of magnetohydrodynamics in bidirectional slip flow of Maxwell fluid subject to stretching, radiation, and variable properties," *Numer. Heat Transf., Part A: Appl.*, vol. 84, no. 1, pp. 1–18, 2023. DOI: 10.1080/10407782.2023.2176383.

[22] N. K. Nayak, "MHD 3D flow and heat transfer analysis of nanofluid by shrinking surface inspired by thermal radiation and viscous dissipation," *Int. J. Mech. Sci.*, vol. 124–125, pp. 185–193, 2017. DOI: 10.1016/j.ijmecsci.2017.03.014.

[23] B. Mahanthesh, B. J. Gireesha, and I. L. Animasaun, "Exploration of non-linear thermal radiation and suspended nanoparticles effects on mixed convection boundary layer flow of nanoliquids on a melting vertical surface," *J. Nanofluids*, vol. 7, no. 5, pp. 833–843, 2018. DOI: 10.1166/jon.2018.1521.

[24] H. Ullah, M. I. Khan, and T. Hayat, "Modeling and analysis of magnet-Carreau fluid with radiative heat flux: dual solutions about critical point," *Adv. Mech. Eng.*, vol. 12, no. 8, pp. 168781402094547, 2020. DOI: 10.1177/1687814020945477.

[25] T. Hayat, H. Ullah, B. Ahmad, and M. S. Alhodaly, "Heat transfer analysis in convective flow of Jeffrey nanofluid by vertical stretchable cylinder," *Int. Commun. Heat Mass Transf.*, vol. 120, pp. 104965, 2021. DOI: 10.1016/j.icheatmasstransfer.2020.104965.

[26] H. B. Lanjwani, M. S. Chandio, M. I. Anwar, S. A. Shehzad, and M. Izadi, "MHD laminar boundary layer flow of radiative Fe-Casson nanofluid: stability analysis of dual solutions," *Chin. J. Phys.*, vol. 76, pp. 172–186, 2022. DOI: 10.1016/j.cjph.2021.10.043.

[27] Y. D. Reddy, F. Mebarek-Oudina, B. S. Goud, and A. I. Ismail, "Radiation, velocity and thermal slips effect toward MHD boundary layer flow through heat and mass transport of Williamson nanofluid with porous medium," *Arab J. Sci. Eng.*, vol. 47, no. 12, pp. 16355–16369, 2022. DOI: 10.1007/s13369-022-06825-2.

[28] M. Z. Swalmeh *et al.*, "Effectiveness of radiation on magneto-combined convective boundary layer flow in polar nanofluid around a spherical shape," *Fractal Fract.*, vol. 6, no. 7, pp. 383, 2022. DOI: 10.3390/fractalfract6070383.

[29] T. Oreyeni, A. Oladimeji Akindele, A. Martins Obalalu, S. Olakunle Salawu, and K. Ramesh, "Thermal performance of radiative magnetohydrodynamic Oldroyd-B hybrid nanofluid with Cattaneo-Christov heat flux model: solar-powered ship application," *Numer. Heat Transf., Part A: Appl.*, pp. 1–19, 2023. DOI: 10.1080/10407782.2023.2213837.

[30] E. M. Sparrow, H. Quack, and C. J. Boerner, "Local nonsimilarity boundary-layer solutions," *AIAA J.*, vol. 8, no. 11, pp. 1936–1942, 1970. DOI: 10.2514/3.6029.

[31] W. J. Minkowycz and E. M. Sparrow, "Local nonsimilar solutions for natural convection on a vertical cylinder," *J. Heat Transf.*, vol. 96, no. 2, pp. 178–183, 1974. DOI: 10.1115/1.3450161.

[32] W. J. Minkowycz and E. M. Sparrow, "Numerical solution scheme for local nonsimilarity boundary-layer analysis," *Numer. Heat Transf., Part B: Fundamentals*, vol. 1, no. 1, pp. 69–85, 1978. DOI: 10.1080/10407797809412161.

[33] M. Hussain and M. Sheremet, "Convection analysis of the radiative nanofluid flow through porous media over a stretching surface with inclined magnetic field," *Int. Commun. Heat Mass Transf.*, vol. 140, pp. 106559, 2023. DOI: 10.1016/j.icheatmasstransfer.2022.106559.

[34] S. Reddy, K. Naikoti, and M. M. Rashidi, "MHD flow and heat transfer characteristics of Williamson nanofluid over a stretching sheet with variable thickness and variable thermal conductivity," *Trans. A. Razmadze Math. Inst.*, vol. 171, no. 2, pp. 195–211, 2017. DOI: 10.1016/j.trmi.2017.02.004.

[35] W. K. Khan and I. Pop, "Boundary-layer flow of a nanofluid past a stretching sheet," *Int. J. Heat Mass Transf.*, vol. 53, no. 11–12, pp. 2477–2483, 2010. DOI: 10.1016/j.ijheatmasstransfer.2010.01.032.

[36] J. K. Madhukesh *et al.*, "Numerical simulation of AA7072-AA7075/water-based hybrid nanofluid flow over a curved stretching sheet with Newtonian heating: a non-Fourier heat flux model approach," *J. Molecular Liquids*, vol. 335, pp. 116103, 2021. DOI: 10.1016/j.molliq.2021.116103.

[37] U. Nazir, M. Sohail, M. B. Hafeez, and M. Krawczuk, "Significant production of thermal energy in partially ionized hyperbolic tangent material based on ternary hybrid nanomaterials," *Energies*, vol. 14, no. 21, pp. 6911, 2021. DOI: 10.3390/en14216911.

[38] I. Tlili, H. A. Nabwey, S. P. Samrat, and N. Sandeep, "3D MHD nonlinear radiative flow of CuO-MgO/methanol hybrid nanofluid beyond an irregular dimension surface with slip effect," *Sci. Rep.*, vol. 10, no. 1, pp. 9181, 2020. DOI: 10.1038/s41598-020-66102-w.

[39] S. Munawar and N. Saleem, "Mixed convective cilia triggered stream of magneto ternary nanofluid through elastic electroosmotic pump: a comparative entropic analysis," *J. Molecular Liquids*, vol. 352, pp. 118662, 2022. DOI: 10.1016/j.molliq.2022.118662.

[40] R. S. Reddy Gorla and I. Sidawi, "Free convection on a vertical stretching surface with suction and blowing," *Appl. Sci. Res.*, vol. 52, no. 3, pp. 247–257, 1994. DOI: 10.1007/BF00853952.

[41] A. M. Megahed, "Williamson fluid flow due to a nonlinearly stretching sheet with viscous dissipation and thermal radiation," *J. Egypt Math. Soc.*, vol. 27, no. 1, pp. 1–10, 2019. DOI: 10.1186/s42787-019-0016-y.